

Metasurface-Enhanced Lab-on-Fiber Biosensors

Marco Consales,* Giuseppe Quero, Sara Spaziani, Maria Principe, Alberto Micco, Vincenzo Galdi, Antonello Cutolo, and Andrea Cusano*

The integration of metasurfaces on the tip of optical fibers enables advanced wavefront manipulations in Lab-on-Fiber application scenarios, and brings about new degrees of freedom that can be exploited for optimizing the surface sensitivity to local variations of the refractive index. Here, a novel biosensing platform is reported based on the integration of a phase-gradient plasmonic metasurface on the tip of an optical fiber, able to detect biomolecular interactions with very high sensitivity. Specifically, the capability of the proposed platform to detect very low concentrations of streptavidin in running buffer solutions, with a limit of detection of the order of a few ng mL^{-1} , is demonstrated. In addition, its inherent integrability within medical catheters/needles renders it potentially very attractive for application scenarios of real-time diagnosis via liquid biopsy at precise locations inside the human body.

1. Introduction

Metamaterials^[1,2] are artificial materials composed of metal or dielectric resonant elements (“meta-atoms”), which derive their optical responses mainly from their structure (rather than the chemical properties of their constituents) and may therefore transcend the limitations of natural materials.^[3–5] In the past two decades, metamaterials have been the subject of a steadily increasing interest in several scientific communities, leading to the demonstration of exotic phenomena such as negative refraction,^[3] superlensing,^[4] and invisibility cloaking,^[6] just to mention a few. More recently, their 2D versions, typically referred to as “metasurfaces” (MSs), have elicited a surge of active research due to a series of promised advantages, including: i) easier realization via traditional nanofabrication techniques such as photolithography and electron-beam lithography; ii) inherent compatibility with on-chip photonics and fiber-optics technology; iii) reduced losses. In essence, a MS is a planar

arrangement of meta-atoms of subwavelength thickness, possibly exhibiting geometric or material modulation in space and/or time.^[7,8] By suitably designing such modulation, it is possible to manipulate the amplitude and/or phase distribution of an optical wavefront within a thickness much smaller than the operational wavelength, thereby enabling flat-optics and photonics applications.^[9,10] Moreover, MSs have been widely investigated in view of their extraordinary capabilities of localized light–matter interaction (see, e.g., refs. [11–13]).

In view of the abovementioned capabilities, MSs have found many applications in scenarios where bulk metamaterials are technologically impracticable,

including beam steering/splitting based on the generalized Snell’s laws,^[14] enhancement of the photonic spin-Hall effect,^[15] aberration-free focusing metalenses,^[16] polarization and angular momentum control,^[17,18] invisibility cloaks,^[19,20] holograms for 3D imaging.^[21]


Of particular interest for the present study is the MS integration with optical fibers, which represents a landmark addition to the arsenal of tools available in the “Lab-on-Fiber” technology,^[22,23] by endowing unprecedented light-manipulation capabilities and setting the stage for development of advanced plug and play devices.^[24,25] More in general, the pervasiveness of the fiber-optic technology may constitute a formidable vehicle for broadening the practical applications of optical MSs to real-world scenarios.

The first demonstration of an “optical fiber meta-tip” (OFMT), i.e., a MS integrated on the tip of an optical fiber, was reported by Principe et al. in 2017.^[26] The proof-of-concept application was the beam steering of a transmitted beam by an arbitrary deflection angle. OFMTs were realized via focused-ion-beam (FIB) milling of arrays of rectangular aperture nanoantennas (rotated by $\pm 45^\circ$ in the plane of the fiber tip) in a gold-coated fiber end-face. In the same study,^[26] it was also experimentally demonstrated that phase-gradient plasmonic MSs driving the deflected beam into the evanescent range could efficiently couple normally incident light into surface waves. This phenomenon was found to yield a stronger field enhancement at the meta-tip surface by comparison with a phase-gradient-free counterpart, experimentally demonstrated through the deposition of a uniform nano-sized overlay.

After this first proof of concept, with emphasis on biosensing scenarios where sensitivity enhancement is pivotal,^[27] we studied how to optimize the surface sensitivity and how to

Dr. M. Consales, Dr. G. Quero, Dr. S. Spaziani, Dr. M. Principe,
Dr. A. Micco, Prof. V. Galdi, Prof. A. Cusano
Department of Engineering
University of Sannio
Benevento 82100, Italy
E-mail: consales@unisannio.it; acusano@unisannio.it

Prof. A. Cutolo
Department of Electrical Engineering and Information Technology
University of Naples “Federico II”
Napoli 80125, Italy

 The ORCID identification number(s) for the author(s) of this article can be found under <https://doi.org/10.1002/lpor.202000180>

DOI: 10.1002/lpor.202000180

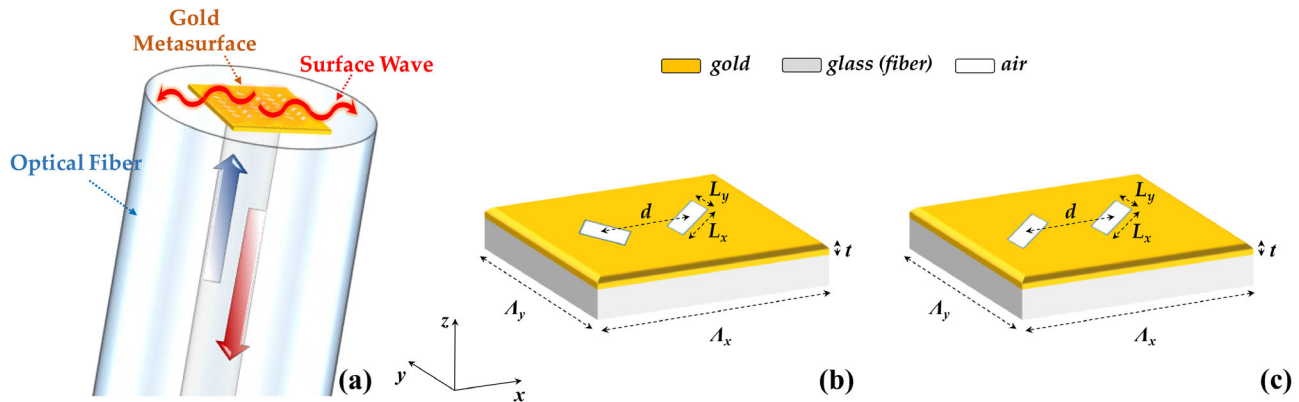


Figure 1. a) Pictorial sketch of the proposed OFMT platform; b,c) geometry of the phase-gradient MS macrocell and its corresponding (gradient-free) benchmark, respectively.

improve the visibility of the resonance. We found that, as described in the present paper, the optimal sensitivity is obtained when the surface wave is excited on both sides of the gold layer, and when the resonance wavelength satisfies particular conditions.

The above results opened up intriguing avenues for the development of extremely high-sensitivity plug and play MS-enhanced biological probes that could potentially outperform available optical-fiber tip (Lab-on-Tip) biosensors,^[28] paving the way to their exploitation for real-time liquid biopsy,^[29–31] possibly performed in vivo.

Other intriguing examples of judicious integration of MSs and optical fibers have been reported in the last two years. For instance, in ref. [32], a 1D grating was integrated, yielding a transmission response with high-quality factor and strong dispersion. In ref. [33], a focusing optical metalens was obtained by patterning a MS on the facet of a photonic-crystal fiber. In ref. [34], a uniform 2D MS was fabricated to implement an all-optical switching device. In ref. [35], a different way of integrating a metalens within an optical fiber was presented for endoscopic optical imaging applications.

So far, however, no attempt has been reported on the application of MS-based optical fiber platforms within the field of biological sensing and, in particular, for liquid biopsy applications.

Here, we demonstrate for the first time, the capability of a suitably designed MS-enhanced Lab-on-Fiber biosensor to significantly outperform a phase-gradient-free plasmonic benchmark in real biological experiments, which may lead to the development of novel advanced optrodes for biosensing. Specifically, using the well-established Biotin–Streptavidin pair as a benchmark, we demonstrate that a device based on a phase-gradient plasmonic MS is able to detect biomolecular interactions with a sensitivity more than two orders of magnitude higher than that provided by a gradient-free counterpart, without adding significant complexity to the design and fabrication. This provides further confirmation of key role played by additional degrees of freedom (e.g., phase gradient) endowed by the MS integration in enhancing the sensing performance, and can pave the way for the development of plasmonic nanoarrays with unprecedented sensing performances. Overall, our results also demonstrate the capability of the realized MS-assisted Lab-on-Fiber biosensor to

detect very low concentrations (on the order of few ng mL^{−1}) of Streptavidin in running buffer solutions.

2. Idea and Geometry

Figure 1a shows the schematic of an OFMT coupling the anomalous, cross-polarized transmitted beam to a surface wave. A Babinet-inverted, plasmonic phase-gradient MS, composed of rectangular aperture resonators milled in a thin gold film, is laid on the flat fiber tip, which is assumed to extend in the transverse (x,y)-plane separating the fiber core (incidence region) and the exterior medium (liquid biological solution). In order to span the entire 2π phase range in the cross-polarized response, the resonators are rotated by 45° in the (x,y)-plane.^[26] By assuming normal incidence and an impressed phase profile varying linearly along the x -direction (and constant along the y -direction), the transmission and reflection angles of the beams ($\theta_{t/r}$) are governed by the generalized Snell's laws^[14]

$$\sin \theta_t = \frac{1}{n_t} \frac{\lambda_0}{2\pi} \gamma, \quad \sin \theta_r = \frac{1}{n_r} \frac{\lambda_0}{2\pi} \gamma \quad (1)$$

where $n_{t/r}$ is the refractive index (RI) of the transmission/incidence region, λ_0 is the operational wavelength, and γ is the (constant) phase gradient. By properly tuning the value of γ , it is possible to attain arbitrary values of $\theta_{t/r}$, thereby transcending the standard Snell's laws. Accordingly, to couple the normally impinging light with a surface wave, we need to exceed the grazing conditions $\theta_t = 90^\circ$ in transmission, and $\theta_r = 90^\circ$ in reflection. From Equation (1), we can readily derive the minimum phase gradient needed, viz.

$$\gamma \geq n_{t/r} \frac{2\pi}{\lambda_0} \quad (2)$$

Equivalently, for fixed γ , we can obtain the minimum wavelength at which the transmitted/reflected field couples to a surface wave (SW), viz.

$$\lambda_{SW}^{t/r} = n_{t/r} \frac{2\pi}{\gamma} \quad (3)$$

which notably coincides with the first Rayleigh anomaly, due to the periodic nature of the structure.^[36] If $\gamma \geq \max\{n_t, n_r\} \frac{2\pi}{\lambda_0}$, both the transmitted and reflected beams couple to surface waves for wavelengths larger than $\max\{\lambda_{sw}^t, \lambda_{sw}^r\}$. The grating nature of the metasurfaces is a key factor since, in conjunction with the impressed linear phase profile, it entails the shift of the transmitted power from the zeroth to the first diffraction order, which reaches the grazing condition in the wavelength range specified above.

Our MS is composed of a macrocell, made by $N \times 1$ antennas, which samples the full 2π phase range, and is repeated along the x - and y -directions. Therefore, any resonator yields a uniform phase difference $\Delta\phi$ in the transmission (and reflection) coefficient with respect to the neighboring elements, given by $\Delta\phi = 2\pi/N$. If $\Lambda_x = Nd$ is the dimension of the macrocell along the x -direction (with the dimension along y being fixed to $\Lambda_y = 1 \mu\text{m}$), the phase gradient is simply $\gamma = \Delta\phi/d = 2\pi/\Lambda_x$.

To achieve the desired high values of the phase gradient, we need to increase the value of the phase sampling step $\Delta\phi$ or, equivalently, to reduce the number N of antennas in a macrocell. The minimum number of antennas per macrocell is two, corresponding to the maximum sampling step, $\Delta\phi = \pi$, allowing a correct reconstruction of the linear phase profile (apart from a sign uncertainty in the gradient). In this case, the two antennas composing the macrocell have equal dimensions, and differ only by a rotation of 90° in the (x,y) -plane, thus rendering the phase shift independent of the operational wavelength.^[37] The geometry of the macrocell is shown in Figure 1b, and the corresponding phase gradient is $\gamma = \pi/d$.

In order to carry out a fair comparative study with a view toward real biosensing scenarios, we also consider a phase-gradient-free benchmark structure consisting of the same antennas but equally oriented (see Figure 1c). Such a benchmark allows to remove the phase-gradient effects while preserving the same gold surface area useful to immobilize the specific bioreceptor, and the inherent response of each individual resonating nanoantenna.

In what follows, by conducting a real biomolecular detection experiment, we assess and compare for the first time the sensing capabilities of a phase-gradient-MS with that of a gradient-free plasmonic benchmark, and we show that the phase gradient is an effective extra degree of freedom which can substantially enhance the sensing performance, without adding any significant complications in the design and fabrication.

2.1. Design Procedure

The geometry described in the previous section is optimized bearing in mind the operational conditions dictated by our biological experiments. In particular, the incidence region is the core of a single-mode optical fiber, i.e., $n_t = 1.45$, the transmission region is a liquid biological solution with a RI $n_r = 1.34$, and the resonance wavelength must lie within the range of 1400–1600 nm, so as to allow the use of standard optoelectronic components for the continuous and real-time interrogation of the plasmonic platforms during the biological experiments.

The thickness of the gold film is chosen as $t = 30 \text{ nm}$, as a good compromise between high sensitivity, low profile,^[38] and capability to support surface plasmon polaritons.^[39] The remain-

ing parameters to be optimized are the antennas' side lengths, L_1 and L_2 , and the distance d between neighboring elements. Based on a preliminary numerical study,^[40] these parameters are tuned so that, at the resonance wavelength λ_r , the grazing condition is satisfied both in transmission and in reflection; this implies that at λ_r , the (constant) phase gradient must be $\gamma \geq \max\{n_t, n_r\} \frac{2\pi}{\lambda_0} = n_r 2\pi/\lambda_0$. Furthermore, in order to improve the quality factor of the resonance, λ_r must be slightly larger than λ_{sw}^r ; this implies the coupling of the antennas' resonance to the lattice surface modes, whose effects have been widely studied in the topical literature.^[41–44]

In particular, to design the structure, we follow two main steps:

Step 1: Setting $d = 1000 \text{ nm}$, we tune the side lengths L_1 and L_2 so that the resonance wavelength lies above the range of interest. Numerical simulations showed that for $d \geq 1000 \text{ nm}$, the reflectivity spectra are mainly affected by the resonance of the single antennas and much more mildly by the array structure.^[40]

Step 2: Having fixed L_1 and L_2 to the values found at step 1, we gradually decrease d , up to its minimum value that allows the MS resonance wavelength to be as close as possible to (but still greater than) λ_{sw}^r . Indeed, as d decreases, the resonance wavelength of the MS blueshifts, so that, at the optimal value of d , the resonance wavelength lies about in the middle of the range of interest.

The gradient-free benchmark configuration is straightforwardly derived from the above design, by orienting all the antennas in a parallel way, and maintaining all other parameters. As previously mentioned, this reference configuration allows to preserve the single antennas' resonant response and the array effects, thereby enabling a fair comparative study to explore the effects of the phase gradient.

3. Results and Discussion

3.1. Probe Design

The initial guess for L_1 and L_2 is obtained via a rough analytical estimate,^[45] and subsequently fine-tuned by numerically computing the resonance wavelength, identified as a dip in the reflected power spectrum. From this analysis, the antenna dimensions are chosen as $L_1 = 300 \text{ nm}$ and $L_2 = 120 \text{ nm}$, yielding a resonance wavelength $\lambda_c \approx 1790 \text{ nm}$ for an interelement spacing $d = 1000 \text{ nm}$. At step 2, the optimal value of d is found to be $d = 500 \text{ nm}$, which yields a spectral resonance centered at 1464 nm (Figure 5a), i.e., right above $\lambda_{sw}^r = 1450 \text{ nm}$. According to our design procedure, at such resonance wavelength, both the transmitted and the reflected cross-polarized beams satisfy the grazing angle condition in Equation (2). For the computation of the reflectivity spectra, we utilize a 2D version of the rigorous-coupled-wave analysis^[46] implemented in a public-domain numerical code (www.sourceforge.net/projects/rcwa-2d/files/); further details can be found in Section S1.1 of the Supporting Information.

The parameters of the designed MS are chosen so as to sustain a resonance in the wavelength range of interest, characterized

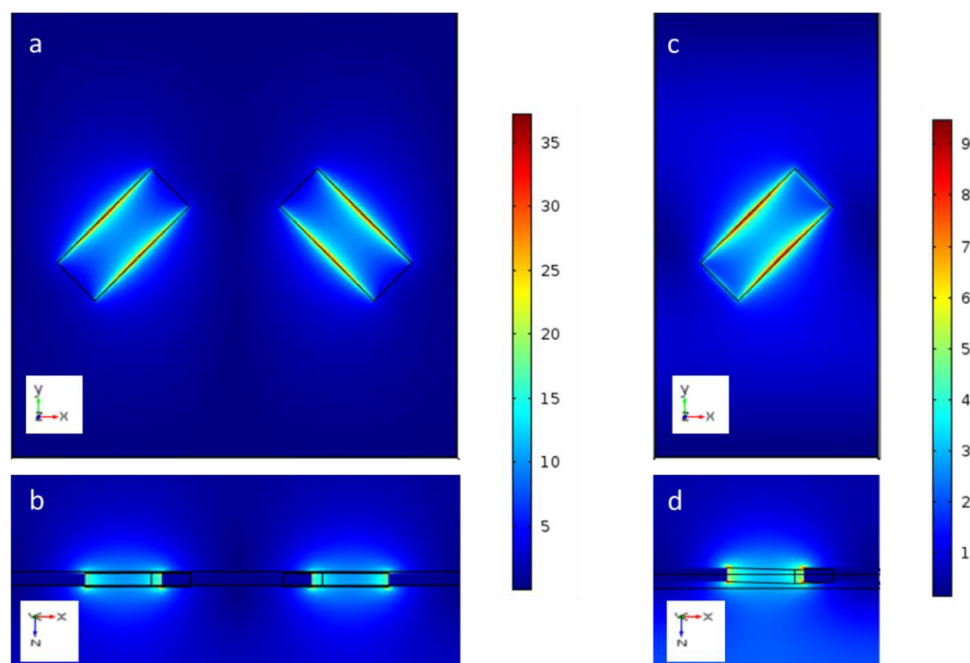


Figure 2. Numerically computed electric field magnitude (normalized with respect to the incident one). a,b) Resonant distributions (at $\lambda = 1472$ nm) in the x - y -plane at 1 nm above the gold surface in the transmission region, and in the x - z -plane at the central y -coordinate of the microcell, respectively, for the phase-gradient OFMT. c,d) Same as panels (a), (b) but for the gradient-free benchmark (at $\lambda = 1422$ nm).

by a strong localization and enhancement of the field due to the plasmonic nature of the phenomenon. As it will be clearer hereafter, this effect is boosted in the presence of the phase gradient.

The resonant field distribution in a phase-gradient MS macrocell, numerically computed via the finite-element-based commercial software COMSOL Multiphysics (www.comsol.com), is shown in **Figure 2a,b**. The incident electric field is assumed to be linearly polarized along the x -direction and to normally impinge on the MS from the optical fiber (further details can be found in Section S1.1 of the Supporting Information). The electric field magnitude (normalized with respect to the incident one) is shown in the x - y -plane at a distance of 1 nm (along z) from the gold surface in the transmission region (Figure 2a), and in the x - z -plane cutting the macrocell at the central y -coordinate (Figure 2b).

The field distribution results from the interplay between the localized waveguide modes supported by the nanoapertures and the surface plasmon polariton mediated by the phase gradient on both sides of the gold layer.^[47] The resonance is designed to be close to the excitation condition of such surface wave, which coincides with the first-order Rayleigh anomaly.^[40]

Note that the polarization of the incident field does not affect the phenomenon under study; we assumed a linearly polarized incident field for a simpler characterization of the fabricated samples. The metasurface exhibits the same behavior also for right/left circularly polarized light,^[37] in which case parallel and orthogonal polarization components become same-sense and reverse-sense circularly polarized components.

For comparison, Figure 2c,d shows the corresponding results for the gradient-free benchmark configuration (at the resonance wavelength $\lambda = 1422$ nm). We observe a qualitatively similar

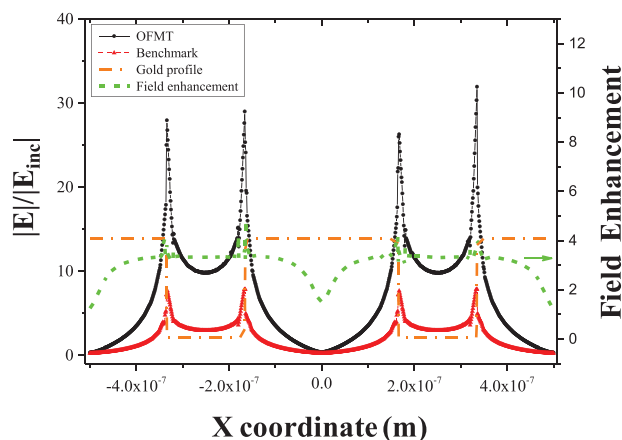


Figure 3. As in Figure 2a,c, but cuts at the central y -coordinate of the macrocell as a function of the x -coordinate for the phase-gradient OFMT (black circles) and the gradient-free benchmark (red triangles); the green dashed curve shows (right axis) the ratio between the two profiles. The position of the nanoaperture is indicated by the orange dash-dotted line.

field distribution, but smaller amplitude. This is quantitatively more evident in **Figure 3**, which compares the cuts at the central y -coordinate from Figure 2a,c, as a function of the x -coordinate. For better visualization, the ratio between the distributions (field enhancement) is also displayed, clearly showing that the phase-gradient OFMT yields a field enhancement, with maximum value of ≈ 3.3 and an average value of ≈ 3 . Another meaningful figure of merit is the integral of field intensity within the sensitive volume involved in biomolecular interaction detection experiments, i.e., a box of 15 nm in thickness over the gold surface covering the entire macrocell. The ratio between such

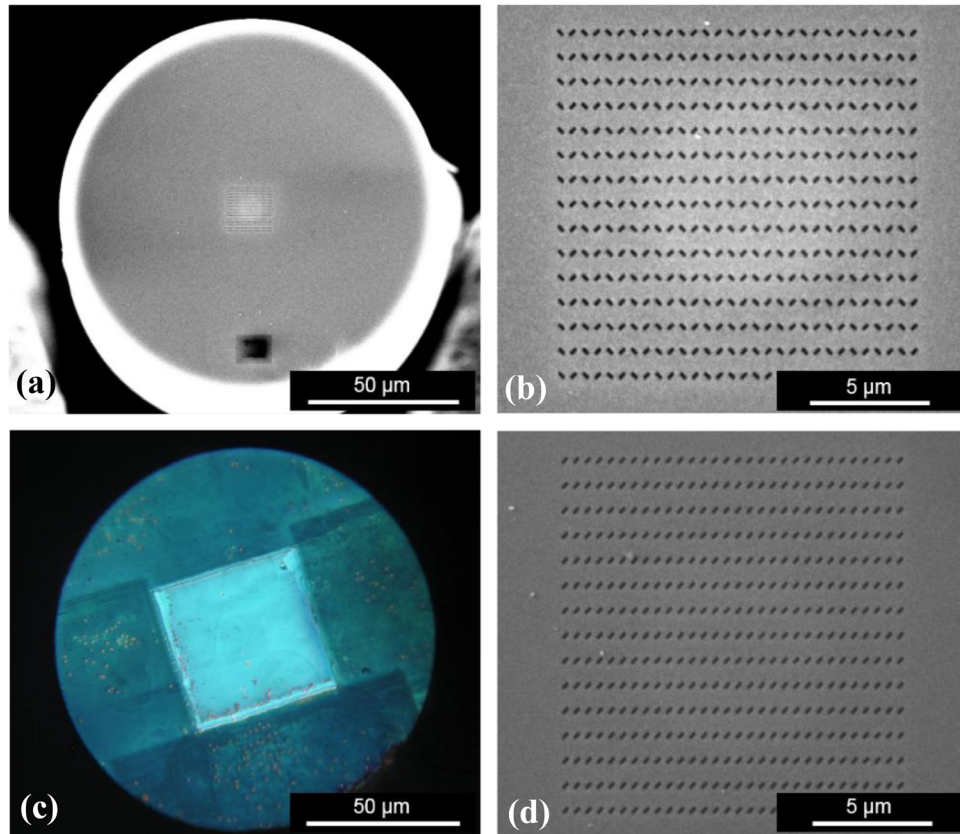


Figure 4. a,b) SEM image and magnified view, respectively, of a fabricated phase-gradient OFMT. c) Optical microscope image of the sample after the gold confinement. d) SEM image of the gradient-free benchmark.

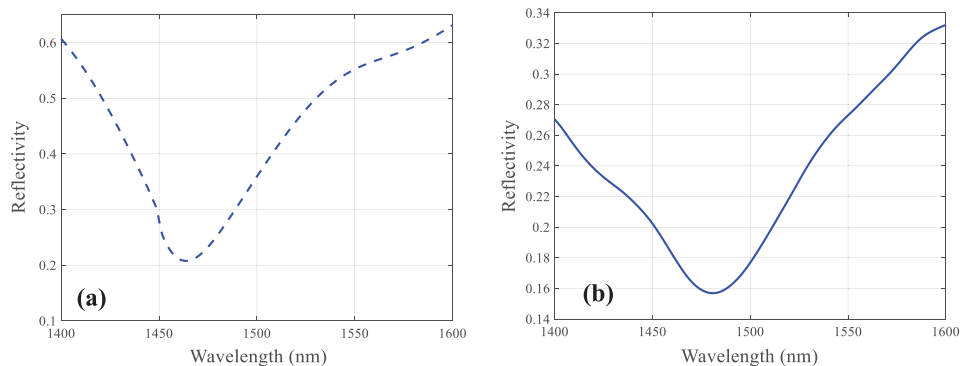


Figure 5. a,b) Simulated and experimental, respectively, reflectivity spectra of the phase-gradient OFMT, for a SRI of 1.333.

volume integrals pertaining to the phase-gradient and gradient-free plasmonic configurations is about 7.7. The field enhancement exhibited by the phase-gradient OFMT is crucial to achieve a higher sensitivity to local variations of the external RI.^[48]

3.2. Probe Fabrication and Characterization

Figure 4a,b shows typical scanning electron microscopy (SEM) images of an OFMT sample, directly realized on the fiber tip. The plasmonic MS (matrix of 30×15 elements) is milled within an $\approx 14 \times 14 \mu\text{m}^2$ area around the core region. An in-depth

analysis carried out both on SEM and atomic force microscopy images indicates that the actual values of the geometrical parameters are slightly larger than the nominal-design ones, with relative errors within the range of 4–9%, in line with previous results.^[26]

Figure 4c shows an optical microscope image of the same sample after the gold confinement process, with the $50 \times 50 \mu\text{m}^2$ gold square clearly visible in the central part of the fiber tip (i.e., around the core). A SEM image of the corresponding gradient-free benchmark is shown in **Figure 4d**.

Figure 5 shows the simulated (panel a) and experimental (panel b) reflectivity spectra pertaining to the phase-gradient

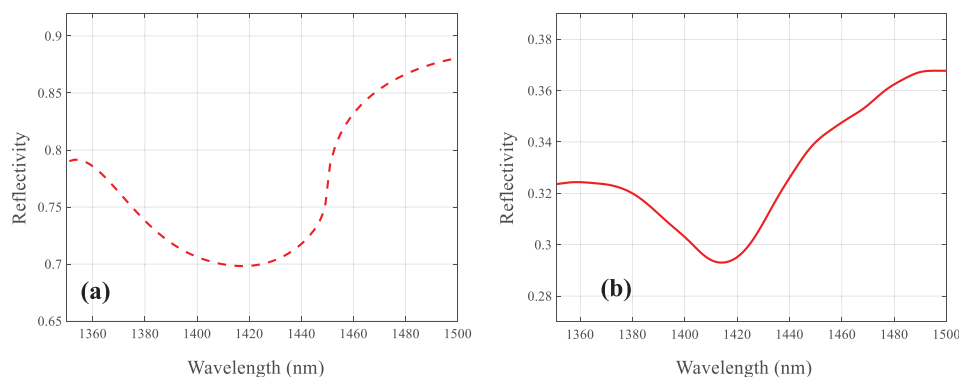


Figure 6. a,b) Simulated and experimental, respectively, reflectivity spectra of the gradient-free benchmark configuration, for a SRI of 1.333.

OFMT for a surrounding refractive index (SRI) of 1.333. Both responses exhibit a sharp resonance dip within the selected wavelength range (i.e., 1400–1600 nm), centered at $\lambda \approx 1464$ nm and $\lambda \approx 1480$ nm, respectively. This slight discrepancy is mainly attributable to the aforementioned fabrication tolerances^[26] and to the finite size of the fabricated structure as opposed to the infinite size of the simulated one.

We point out that the measured (and simulated) reflectivity accounts for the total reflected power. However, when the surface wave condition is satisfied, there is only one propagating diffracted order with polarization orthogonal to the incident one.

Qualitatively similar results are observed for the gradient-free benchmark configuration, as shown in **Figure 6**. In this case, a smaller discrepancy of about 3 nm was observed between the theoretically computed and experimentally measured resonance dip ($\lambda \approx 1417$ nm and $\lambda \approx 1414$ nm, respectively).

3.3. Plasmonic Probe Biofunctionalization

With reference to the biological protocol adopted for the molecular interaction experiments (described in detail in the Experimental Section), **Figure 7** shows a typical real-time sensorgram obtained during the phase-gradient OFMT biofunctionalization phase. Specifically, it displays the time variation of resonant wavelength shift ($\Delta\lambda_c$) during both the bioreceptor (Biotin) immobilization on the meta-tip surface and the blocking step in bovine serum albumin (BSA). It is worth pointing out that the first steps of piranha cleaning and thiol incubation on the meta-tip surface are performed overnight, without monitoring the wavelength shift.

The OFMT probe is initially dipped in a phosphate buffered saline (PBS) (Sigma-Aldrich) solution at room temperature (RT) (**step I**). Subsequently, it is immersed for ≈ 2 h in the *N*-hydroxysuccinimide (NHS)–Biotin solution (Thermo Fisher), leading to a redshift of the optical signal of about 0.8 nm (**step II**). This variation is mostly due to the differences between the bulk RI of the Biotin solution ($n_{\text{Biotin}} = 1.3362$, at $\lambda = 589$ nm) and the PBS one ($n_{\text{PBS}} \approx 1.3346$, at $\lambda = 589$ nm). To avoid any influence of bulk RI change due to solutions of different compositions, and to estimate the net contribution of Biotin adsorption, the probe is removed from the Biotin solution and rapidly immersed again in

a clean PBS. By comparing the $\Delta\lambda_c$ recorded in PBS before (**step I**) and after (**step III**) the bioreceptor immobilization, a small but non-negligible variation in $\Delta\lambda_c$ is observed ($\Delta\lambda_{c-\text{Biotin}} = 0.15$ nm), thus revealing the MS-assisted biosensor capability to detect the formation of a very thin layer of Biotin on the OFMT surface.

The blocking step is performed by immersing the OFMT probe in a 3% solution of BSA for ≈ 40 min (**step IV**), recording a redshift for the optical signal of ≈ 1 nm. Again, to estimate the net contribution of BSA adsorption, the probe is removed from the BSA (Sigma-Aldrich) solution and rapidly immersed in PBS (**step V**), observing a $\Delta\lambda_{c-\text{BSA}} \approx 0.1$ nm.

Figure 8 shows the corresponding results for the gradient-free benchmark configuration. In this case, the resonant wavelength λ_c shifts similarly when the device is immersed within the different biological solutions, but it does not exhibit significant variations due to the anchoring of the Biotin ($\Delta\lambda_{c-\text{Biotin}} \approx 0$) and/or of the BSA molecule ($\Delta\lambda_{c-\text{BSA}} \approx 0$) on the gold-coated surface. This result represents a first evidence of the phase-gradient OFMT capability to outperform its gradient-free counterpart in a realistic biological sensing scenario, which stems from the enhanced light–matter interaction occurring at the meta-tip surface.

3.4. Quantitative Detection of Biotin/Streptavidin Interaction

Once performed the plasmonic probe biofunctionalization, we focus on the Streptavidin detection tests. **Figure 9a** shows the real-time sensorgram pertaining to the phase-gradient OFMT biosensor during a typical experiment performed at RT by means of three different PBS solutions with Streptavidin concentrations of 25 ng mL^{−1}, 250 ng mL^{−1}, and 2.5 $\mu\text{g mL}^{-1}$ (Sigma-Aldrich). It is worth pointing out that the three tested sample solutions are characterized by the same bulk RI of PBS (i.e., 1.3346, at $\lambda = 589$ nm), due to their very low Streptavidin concentration. Also shown, in **Figure 9b**, is the sensorgram pertaining to the reference probe during the negative control test.

Both probes are initially dipped in PBS (**steps I, III, and V**) and subsequently immersed and incubated for 1 h within the sample solutions to promote analyte capture (**steps II, IV, and VI**) (green, cyan, and red markers). Right after the immersion, Streptavidin molecules bind to the Biotin immobilized on the surface of biofunctionalized probe, thus promoting an increase of the local RI and, in turn, a redshift in the resonant wavelength λ_c (**Figure 9c**).

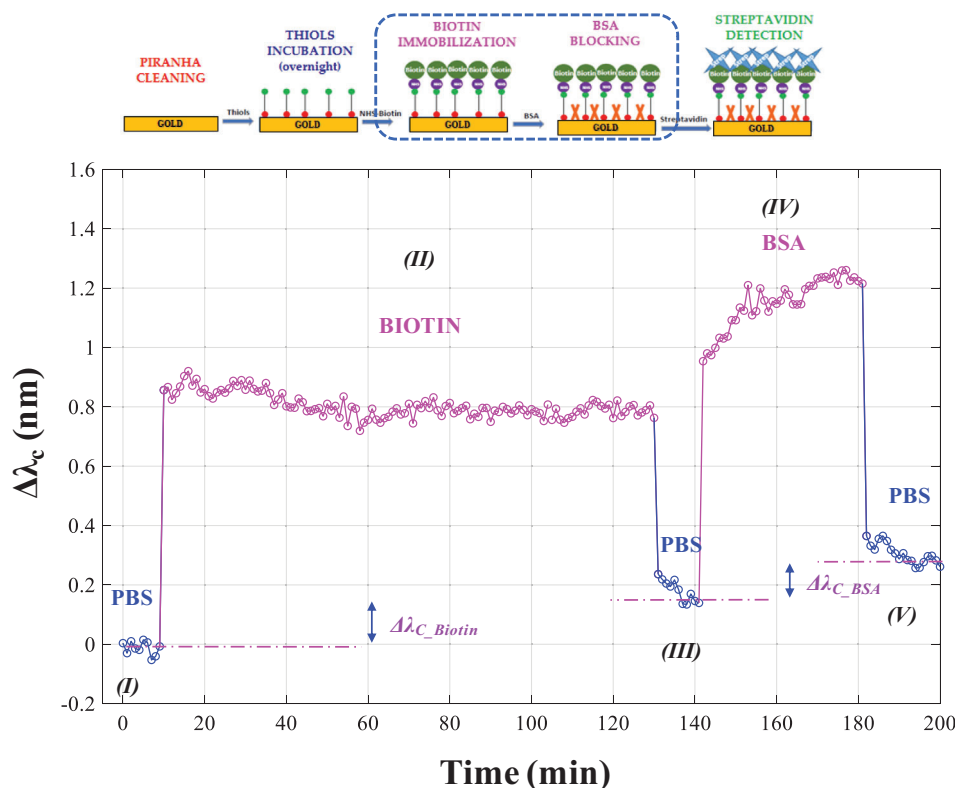


Figure 7. Typical real-time sensorgram showing the phase-gradient OFMT resonant wavelength shift ($\Delta\lambda_c$) during the biofunctionalization phase. A pictorial sketch of the biological protocol is also reported at the top of the figure.

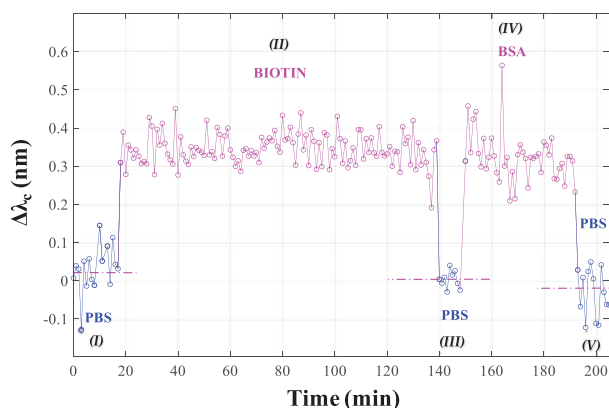


Figure 8. As in Figure 7, but for the gradient-free benchmark configuration.

As expected, and evident from Figure 9b, the immersion of the reference probe (with no Biotin on its surface) in the three tested solutions yields negligible variations in the measured optical signal, except for a slight drift toward smaller wavelengths, also visible in Figure 9a.

In order to record, for each concentration, either the binding and dissociation dynamics, after the incubation, the OFMT probe is rinsed in clean PBS (**steps III, V, and VII**). The observed dissociation dynamics ($\Delta\lambda_{c-III-II}$, $\Delta\lambda_{c-V-IV}$, and $\Delta\lambda_{c-VII-VI}$) are very moderate (≤ 0.08 nm) by comparison with the binding ones,

this effect resulting from the very high affinity of the Biotin–Streptavidin pair.

Furthermore, as expected, the higher the Streptavidin concentration, the greater the number of binding sites being occupied by the target molecule on the OFMT surface, the higher $\Delta\lambda_c$ by comparison with the unoccupied surface ($\Delta\lambda_{c-III-I}$, $\Delta\lambda_{c-V-I}$, and $\Delta\lambda_{c-VII-I}$). Specifically, $\Delta\lambda_c$ values of about 0.5, 1.0, and 1.6 nm are observed for Streptavidin concentrations of 25 ng mL^{−1}, 250 ng mL^{−1}, and 2.5 μg mL^{−1}, respectively.

Figure 10a shows the corresponding results for the gradient-free benchmark configuration for the same biological experiment as in Figure 9a. In this case, the experiment is conducted by using two samples with the highest Streptavidin concentration, i.e., 250 ng mL^{−1} and 2.5 μg mL^{−1}.

Notably, different from what observed in Figure 9a, the gradient-free benchmark probe is not capable of detecting any Biotin–Streptavidin interaction when immersed in the PBS solution with a Streptavidin concentration of 250 ng mL^{−1} (**step II**), whereas a resonant wavelength shift of ≈ 0.3 nm is observed only for the highest concentration of 2.5 μg mL^{−1} (**step IV**), about 5 times smaller than that provided by the phase-gradient MS-enhanced biosensor at the same concentration. This is essentially a consequence of the stronger light–matter interaction provided by the phase-gradient MS on the fiber tip in comparison with the gradient-free counterpart, in line with the aforementioned numerical evidence of the field enhancement experienced within the sensitive volume involved in biomolecular interaction detection experiments (i.e., up to 15 nm away from the probe's

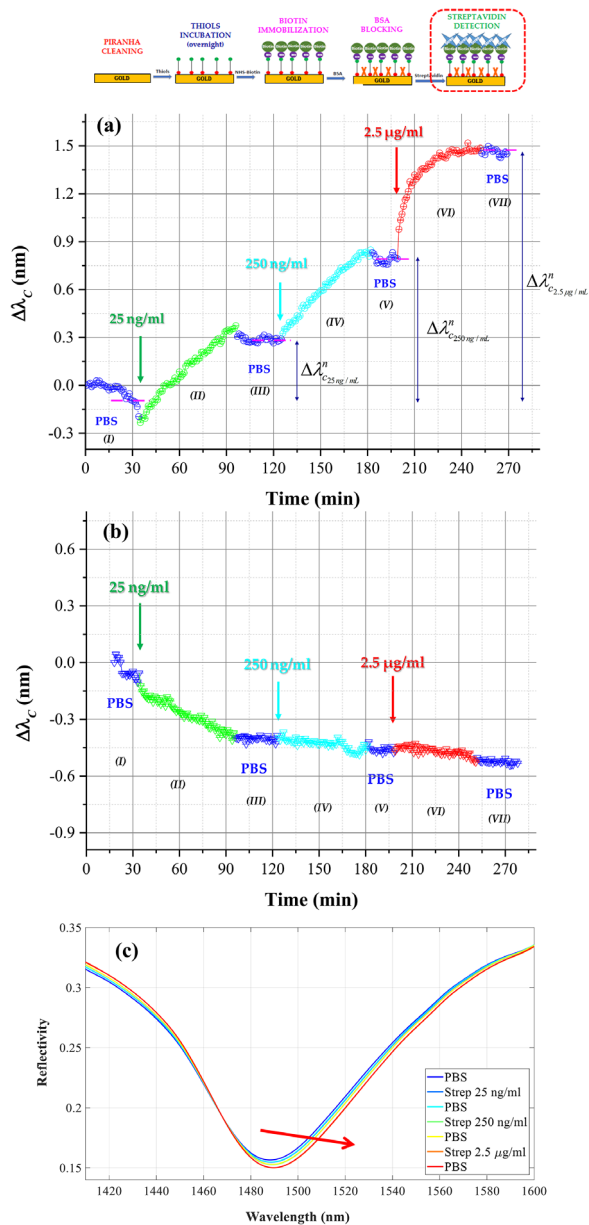


Figure 9. a,b) Real-time sensorgrams pertaining to a Biotin–Streptavidin interaction experiment performed, at RT, using three PBS solutions with increasing Streptavidin concentrations, for the functionalized and non-functionalized (reference) phase-gradient OFMT probes, respectively. c) OFMT steady-state reflectivity spectra for PBS solutions and sample solutions with increasing Streptavidin concentrations. A pictorial sketch of the biological protocol is also reported at the top of the figure.

gold-coated surface). Indeed, it is well-known that the resonance shift and, hence, the sensitivity strongly depends on the overlap between the electromagnetic field intensity at the sensor surface and the layer of immobilized target molecules.

Figure 11 compares the dose–response curves of the proposed phase-gradient and gradient-free biosensing platforms within the Streptavidin concentration range of 2.5 ng mL^{−1}–2.5 $\mu\text{g mL}^{-1}$, prepared and tested in the same experimental conditions. Experiments are performed in triplicates, and cumulative values are

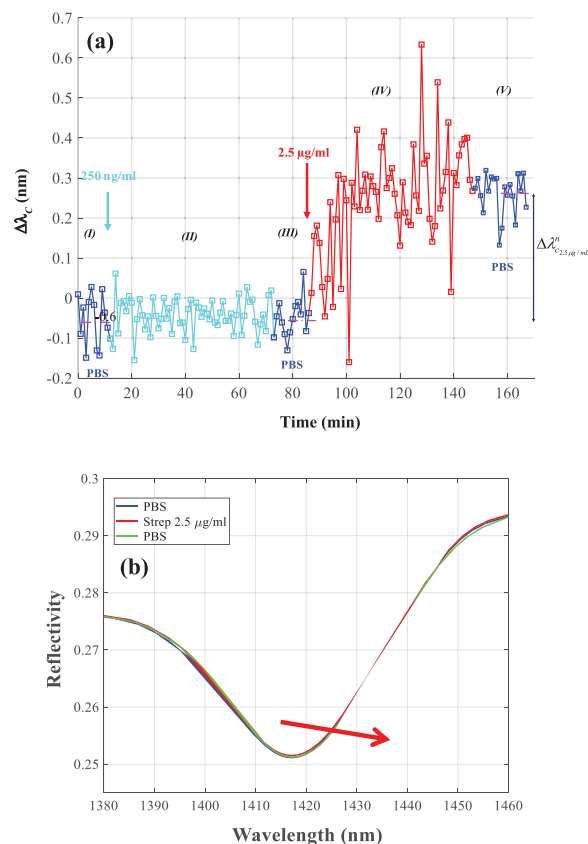


Figure 10. a) As in Figure 9b, but for the gradient-free benchmark configuration. b) Steady-state reflectivity spectra for PBS “before” (blue curve), sample solution with Streptavidin concentration of 2.5 $\mu\text{g mL}^{-1}$ (red curve) and PBS “after” (green curve).

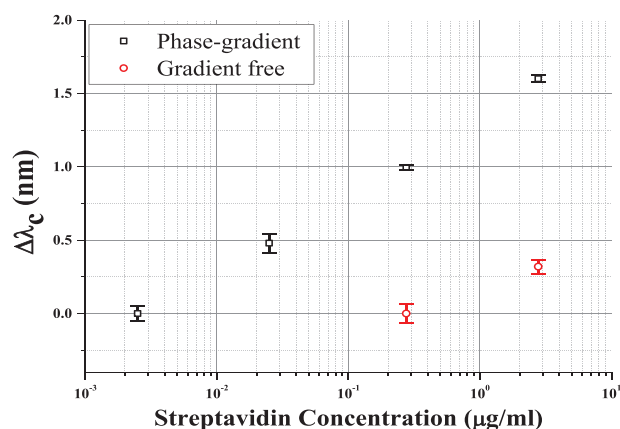


Figure 11. Dose–response curves pertaining to the phase-gradient OFMT (black squares) and gradient-free benchmark (red circles) biosensing platforms, obtained as a result of three different tests for each Streptavidin concentration.

considered when a probe previously tested with a lower concentration is reused for a higher concentration experiment (as the case shown in Figure 9).

As evidenced by the semi-log scale, the dose–response curve pertaining to the phase-gradient OFMT probe exhibits a

logarithmic behavior, thus revealing a saturation phenomenon that can be attributed to the gradual saturation of the available binding sites (Biotin) on the meta-tip surface.

A rough estimation of the limit of detection (LOD) against Streptavidin can be performed by considering its sensitivity in the low concentration range of 2.5–25 ng mL⁻¹

$$S_{LC} = \delta\lambda_c / \delta C_{Strep} \approx 20 \times 10^{-12} \text{ m} / (\text{ng mL}^{-1}) \quad (4)$$

The LOD can be then obtained by dividing by S_{LC} the minimum detectable value for the optical signal, evaluated as the maximum standard deviation (shown as error bars in Figure 11) in the considered range ($\sigma_{Max} \approx 65 \times 10^{-12} \text{ M}$)^[49,50]

$$\text{LOD} = \frac{\sigma_{Max}}{S_{LC}} \approx 3 \text{ ng mL}^{-1} \quad (5)$$

corresponding to $\approx 50 \times 10^{-12} \text{ M}$.

By performing the same procedure for the gradient-free benchmark, the sensitivity turns out to be $\approx 0.13 \times 10^{-12} \text{ M}/(\text{ng mL}^{-1})$, thus yielding a LOD $\approx 380 \text{ ng mL}^{-1}$.

The detection capability of our proposed phase-gradient OFMT biosensor, therefore, turns out to be over two orders of magnitude higher than its gradient-free counterpart, thereby providing further evidence of the great beneficial effects of phase gradient on the biological sensing performance of plasmonic nanoarrays. It is worth emphasizing that these beneficial effects essentially come at no cost, from both the design and fabrication viewpoints.

3.5. Comparison with the State of the Art

In order to comparatively assess the degree of performance of our proposed Lab-on-Fiber platforms, we carry out an analysis of the state-of-the-art of fiber-optic biosensors for the detection of Streptavidin in liquid samples. Results in terms of limit of detection are summarized in Table 1.

It is evident that the proposed phase-gradient OFMT biosensing platform exhibits one of the best sensing performances, and its LOD is only outperformed by a surface-plasmon-resonance biosensor based on a 1 cm long gold-coated tilted fiber Bragg grating (TFBG).^[51]

Table 1. Figures of merit for state-of-the-art fiber-optic Streptavidin biosensors.

Biosensing platform	Limit of detection	Ref.
Gold-coated tilted fiber Bragg gratings	120 pg mL ⁻¹ ($2 \times 10^{-12} \text{ M}$)	[51]
Phase-gradient OFMT	3 ng mL ⁻¹ ($50 \times 10^{-12} \text{ M}$)	This work
LPG in transition mode	75 ng mL ⁻¹ ($1.25 \times 10^{-9} \text{ M}$)	[52]
Gradient free benchmark	380 ng mL ⁻¹ ($6.4 \times 10^{-9} \text{ M}$)	This work
Multimode optical fiber	6 μg mL ⁻¹ ($100 \times 10^{-9} \text{ M}$)	[53]
Photonic crystal fiber	10 μg mL ⁻¹ ($167 \times 10^{-9} \text{ M}$)	[54]
Turnaround point long period gratings	12 μg mL ⁻¹ ($200 \times 10^{-9} \text{ M}$)	[55]
Multimode optical fiber	1.5 mg mL ⁻¹ ($29 \times 10^{-6} \text{ M}$)	[56]

Specifically, the LOD provided by the OFMT biosensor is about one order of magnitude larger than the one provided by the TFBG-based device (50×10^{-12} vs $2 \times 10^{-12} \text{ M}$) which, however, is characterized by an active surface ($\approx 4 \text{ mm}^2$) more than three orders of magnitude larger ($\approx 2.5 \times 10^{-3} \text{ mm}^2$).

It is worth emphasizing that the biosensor size reduction leads to significant advantages in practical (on-field) biosensing applications, in terms of both smaller sample volumes required for the analysis and increased binding efficiency for the target molecule.^[57,58]

In addition, due to the peculiar TFBG transmission-mode configuration and its inherent sensitivity to bending, the development of appropriate strain-free packages is mandatory to host the TFBG-based device during biological experiments, to avoid that bending applied on the TFBG can introduce unexpected variations in its transmitted spectrum, thus complicating the sensor signal interpretation. On this line of argument, the capability of the proposed MS-enhanced device to operate in reflection mode addresses the mentioned issues, and allows its easy integration in the vials containing the biological solution, thus representing a more practical and robust solution to be employed for real-world biological applications.^[59–61] More important, the transmission-mode configuration prevents the integration of TFBG-based devices in medical needles/catheters and, consequently, their exploitation for in vivo applications. Moreover, the transmission mode operation poses severe limits also to an efficient integration in microfluidics platforms for point-of-care development. On the contrary, the inherent integrability of the proposed platform within medical catheters/needles or microfluidic platforms makes it potentially very attractive for application scenarios of real-time diagnosis via liquid biopsy at precise locations inside the human body. Finally, compared to the TFBG-based devices, the fabrication process of the proposed device is simpler and, above all, scalable for high throughput fabrication using a proper holder combined with an absolute coordinate system equipped with a high precision stage.

We point out that, in spite of the anticipated deteriorations, the gradient-free benchmark device too reaches a respectable position in the performance ranking, demonstrating its capability to detect Streptavidin with detection limits ($\approx 6 \times 10^{-9} \text{ M}$) comparable with or even smaller than those provided by other state-of-the-art Lab-on-Fiber biosensors, such as long-period-grating-based devices (1.25×10^{-9} and $200 \times 10^{-9} \text{ M}$).^[52,55] multimode optical fiber-based probes (LOD $\geq 100 \times 10^{-9} \text{ M}$)^[53,56] and photonic crystal fiber biosensors ($29 \times 10^{-6} \text{ M}$).^[54,55]

Such results further emphasize the beneficial effects induced by the phase gradient in the design and development of plasmonic nanoarrays, in terms of significant field enhancements and, consequently, major improvements in their sensing performance.

4. Conclusions

We have demonstrated for the first time that “Lab-on-Fiber” optrodes based on phase-gradient plasmonic MSs integrated on the tip of an optical fiber can significantly outperform standard (phase-gradient-free) plasmonic benchmarks in real biological experiments involving the detection of nanoscale molecular interactions.

Specifically, we have shown that our proposed MS-enhanced biosensor is able to detect Biotin–Streptavidin interactions with a sensitivity over two orders of magnitude higher than that of a gradient-free counterpart. Such higher sensitivity is mainly attributable to the phase gradient, which improves the coupling of the incident field to the plasmonic resonance, thus yielding a higher field enhancement, and comes at a negligible design and fabrication cost.

Moreover, this improvement is independent on the antenna geometry. Thus, we expect that adopting antennas capable of yielding a larger enhancement of the local field in conjunction with the phase gradient might provide unprecedented sensing performances.

Our results also demonstrated the capability of the proposed biosensor to detect very low concentrations of Streptavidin in running buffer solutions with a sensitivity of $\approx 20 \times 10^{-12} \text{ M}/(\text{ng mL}^{-1})$ and a limit of detection as low as 3 ng mL^{-1} ($\approx 50 \times 10^{-12} \text{ M}$).

Compared with state-of-the-art fiber optic biosensors for the detection of Streptavidin in liquid samples, our platform exhibits one of the best sensing performances, with a LOD only one order of magnitude larger than that of a surface-plasmon-resonance biosensor with a much larger (over three orders of magnitude) active surface.

Overall, these outcomes open up intriguing perspectives in the chemo-biosensing field, and in particular for the development of plug and play “Lab-on-Tip” optrodes for the real-time quantitative detection of clinically relevant biotargets.^[62–65] In this context, the exploration of the sensing capabilities of the developed platform for the real-time detection of cancers and infectious biomarkers is also of great interest, and is currently being pursued.

Smart fabrics and textiles represent another intriguing domain where the proposed platform can naturally be implemented, exploiting its easiness in weaving within the filaments of the fabrics, thus enabling the monitoring of the biochemical parameters of the person wearing them.^[66,67]

Finally, we remark that “Lab-on-Tip” optrodes are particularly apt to the integration within medical catheters/needles, thus allowing the development of plug and play devices able to perform biological assays directly in vivo. For instance, one can envision to carry out liquid biopsy at precise locations inside the human body, possibly providing real-time diagnosis.^[29–31]

5. Experimental Section

Prototype Fabrication: For the fabrication of both plasmonic prototypes (phase-gradient OFMT and gradient-free benchmark), a standard single mode fiber (Corning SMF-28) was cleaved and rinsed with ethanol to obtain a smooth surface. A 30 nm gold layer was deposited on the fiber tip by means of an electron beam evaporator (Kenosistec CL400C, Binasco (MI), Italy), with an intermediate 2 nm titanium layer exploited to facilitate the gold adhesion to the fiber surface. The designed pattern was milled into the gold layer by a FIB (Quanta 200 3D FEI, Hillsboro, OR, USA), using a current of 50 pA and an accelerating voltage of 30 kV. The single write field was written with a magnification of 5000 \times using a parallel milling strategy which relied on a source text code where all the rectangular holes were defined in terms of size, spatial coordinates, and rotation angles. Finally, the gold layer around the patterned area (typically $\approx 15 \times 15 \mu\text{m}^2$)^[26] was ablated so as to leave on the fiber tip a $50 \times 50 \mu\text{m}^2$ gold square centered around the core. This allowed to reduce (of about one

order of magnitude) the gold active surface available for thiol incubation (and, consequently, for recognition element immobilization), thus resulting in an increased binding efficiency.^[57] The ablation process was performed by means of an excimer laser (LB 1000, Optec, Belgium) working at a wavelength of 248 nm, with a pulse width of about 5–6 ns. A plastic holder kept the optical fiber facet perpendicular to the laser beam during the ablation process. The laser energy used was 3 mJ and the repetition rate was 50 Hz.

Prototype Characterization: The spectral (reflectivity) characterization of the realized samples was performed by means of a well-established optoelectronic setup (shown in Figure S2 in the Supporting Information). Specifically, the device was illuminated with a broadband polarized optical source and the reflected light was redirected (via a 1×2 directional coupler) to an optical spectrum analyzer. The acquired reflectivity spectrum was normalized by that of the source (SLED 1550D5A, OptoSpeed, Switzerland), obtained by measuring the light reflected by a reference mirror fabricated by depositing a 160 nm thick gold film on the facet of a standard single-mode fiber. During the biological experiments, a setup employing two optical spectrum analyzers (OSAs) was used (shown in Figure S3 in the Supporting Information), and the reflectivity spectrum was obtained by the ratio between the reflectivity spectrum of the device (acquired by OSA 1, AQ6317C, ANDO, Japan) and the one simultaneously emitted by the source (acquired by OSA 2, AQ6315B, ANDO, Japan), normalized with respect to the transfer functions of the 2×2 directional coupler paths.

The reflectivity spectra were transferred (via a general purpose interface bus connection) to a personal computer for postprocessing, mainly filtering and real-time detection of the resonance barycentric wavelength λ_c . During the experiments, the reflection spectrum of the device was automatically acquired every 60 s, thereby providing a continuous and real-time monitoring of the target biological molecule interaction kinetics.

Plasmonic Platform Functionalization and Bioassay Protocol: In order to achieve an effective and selective recognition of the target biomolecules (i.e., Streptavidin), the active gold-coated surface of the plasmonic probes needed to be properly functionalized with a specific and affine bioreceptor (Biotin). Clearly, for a meaningful comparison, the same biofunctionalization needed to be carried out for the phase-gradient OFMT and its corresponding gradient-free benchmark.

The biofunctionalization protocol was first optimized by Enzyme-Linked Immunosorbent Assay (ELISA) experiments performed on gold-coated microscopy slides (see Section S1.2 of the Supporting Information for more details), and subsequently transferred to the plasmonic Lab-on-Fiber platforms. Specifically, with reference to the pictorial sketches reported at the top of Figures 7 and 9, the probes were first cleaned in a piranha solution and washed in MilliQ water and ethanol (EtOH). Afterward, they were immersed in a solution of thiol–poly ethylene glycol–amine (SH–PEG–NH₂ – Thermo Fisher) at $1 \times 10^{-3} \text{ M}$ in EtOH overnight at 4 °C to form an ordered self-assembled monolayer of amino groups on their gold-coated surface, useful for the subsequent Biotin attachment. It was pointed out that the choice of SH–PEG–NH₂ as a functionalized layer allowed to minimize the distance of the Biotin from the gold surface ($\approx 10 \text{ nm}$), thus exploiting a much stronger field in its close proximity. The probes were then rinsed with EtOH and immersed in N-hydroxysuccinimide–Biotin (NHS–Biotin – Thermo Fisher) freshly prepared at $500 \mu\text{g mL}^{-1}$ phosphate buffered saline pH 7.4 (PBS buffer – Sigma-Aldrich) at 4 °C for 2 h.

In order to minimize nonspecific Streptavidin adsorption and to cover potentially uncoated areas of the sensor surface, a blocking step was also performed by immersing the probes in BSA solution 3% w/v in PBS buffer for 40 min.

Subsequently, a dose-response assay was performed by means of several biofunctionalized probes (both OFMTs and gradient-free benchmark) to obtain a calibration curve for the quantitative detection of Streptavidin (S0677 – Sigma-Aldrich). To this aim, the realized devices were dipped into different samples of PBS solutions with Streptavidin concentration ranging from 2.5 ng mL^{-1} to $2.5 \mu\text{g mL}^{-1}$ (corresponding to the range of 41.7×10^{-12} – $41.7 \times 10^{-9} \text{ M}$), and the observed variation of λ_c ($\Delta\lambda_c$) recorded in real time.

To verify (and quantify) the existence of eventual nonspecific bindings to the gold-coated probe surface, a negative control test was also performed by means of a further OFMT probe prepared in the same way but without the attachment of NHS–Biotin (reference probe).

Supporting Information

Supporting Information is available from the Wiley Online Library or from the author.

Acknowledgements

M.C. and G.Q. contributed equally to this work.

Conflict of Interest

The authors declare no conflict of interest.

Keywords

biomolecular sensing, lab-on-fiber technology, label-free fiber optic biosensors, optical fiber meta-tips, phase-gradient metasurfaces

Received: April 28, 2020

Revised: July 8, 2020

Published online:

- [1] F. Capolino, *Metamaterials Handbook*, CRC Press, Boca Raton, FL 2009.
- [2] W. Cai, V. M. Shalaev, *Optical Metamaterials: Fundamentals and Applications*, Springer, Cham 2016.
- [3] D. R. Smith, W. J. Padilla, D. C. Vier, S. C. Nemat-Nasser, S. Schultz, *Phys. Rev. Lett.* **2000**, *84*, 4184.
- [4] J. B. Pendry, *Phys. Rev. Lett.* **2000**, *85*, 3966.
- [5] J. Valentine, S. Zhang, T. Zentgraf, E. Ulin-Avila, D. A. Genov, G. Bartal, X. Zhang, *Nature* **2008**, *455*, 376.
- [6] D. Schurig, J. J. Mock, B. J. Justice, S. A. Cummer, J. B. Pendry, A. F. Starr, D. R. Smith, *Science* **2006**, *314*, 977.
- [7] J. B. Pendry, D. Schurig, D. R. Smith, *Science* **2006**, *312*, 1780.
- [8] Y. Hadad, D. L. Sounas, A. Alu, *Phys. Rev. B* **2015**, *92*, 100304.
- [9] A. V. Kildishev, A. Boltasseva, V. M. Shalaev, *Science* **2013**, *339*, 1232009.
- [10] N. Yu, F. Capasso, *Nat. Mater.* **2014**, *13*, 139.
- [11] X. Luo, *Adv. Opt. Mater.* **2018**, *6*, 1701201.
- [12] S. Chen, W. Liu, Z. Li, H. Cheng, J. Tian, *Adv. Mater.* **2020**, *32*, 2070022.
- [13] L. Kang, R. P. Jenkins, D. H. Werner, *Adv. Opt. Mater.* **2019**, *7*, 1801813.
- [14] N. Yu, P. Genevet, M. A. Kats, F. Aieta, J.-P. Tetienne, F. Capasso, Z. Gaburro, *Science* **2011**, *334*, 333.
- [15] X. Yin, Z. Ye, J. Rho, Y. Wang, X. Zhang, *Science* **2013**, *339*, 1405.
- [16] F. Aieta, M. A. Kats, P. Genevet, F. Capasso, *Science* **2015**, *347*, 1342.
- [17] N. Yu, F. Aieta, P. Genevet, M. A. Kats, Z. Gaburro, F. Capasso, *Nano Lett.* **2012**, *12*, 6328.
- [18] R. C. Devlin, A. Ambrosio, N. A. Rubin, J. P. B. Mueller, F. Capasso, *Science* **2017**, *358*, 896.
- [19] X. Ni, Z. J. Wong, M. Mrejen, Y. Wang, X. Zhang, *Science* **2015**, *349*, 1310.
- [20] L. Y. Hsu, T. Lepetit, B. Kante, *Prog. Electromagn. Res.* **2015**, *152*, 33.
- [21] P. Genevet, F. Capasso, *Rep. Prog. Phys.* **2015**, *78*, 024401.
- [22] A. Cusano, M. Consales, A. Crescitelli, A. Ricciardi, *Lab-on-Fiber Technology*, Springer Series in Surface Sciences, vol. 56, Springer International Publishing, Cham, Switzerland **2015**, ISBN 978-3-319-06998-2.
- [23] M. Consales, M. Pisco, A. Cusano, *Photonic Sens.* **2012**, *2*, 289.
- [24] M. Consales, A. Ricciardi, A. Crescitelli, E. Esposito, A. Cutolo, A. Cusano, *ACS Nano* **2012**, *6*, 3163.
- [25] A. Ricciardi, M. Consales, G. Quero, A. Crescitelli, E. Esposito, A. Cusano, *ACS Photonics* **2014**, *1*, 69.
- [26] M. Principe, M. Consales, A. Micco, A. Crescitelli, G. Castaldi, E. Esposito, V. L. Ferrara, A. Cutolo, V. Galdi, A. Cusano, *Light: Sci. Appl.* **2017**, *6*, e16226.
- [27] A. Ricciardi, A. Crescitelli, P. Vaiano, G. Quero, M. Consales, M. Pisco, E. Esposito, A. Cusano, *Analyst* **2015**, *140*, 8068.
- [28] P. Vaiano, B. Carotenuto, M. Pisco, A. Ricciardi, G. Quero, M. Consales, A. Crescitelli, E. Esposito, A. Cusano, *Laser Photonics Rev.* **2016**, *10*, 922.
- [29] E. Crowley, F. D. Nicolantonio, F. Loupakakis, A. Bardelli, *Nat. Rev. Clin. Oncol.* **2013**, *10*, 472.
- [30] J. D. Cohen, L. Li, Y. Wang, C. Thoburn, B. Afsari, L. Danilova, C. Douville, A. A. Javed, F. Wong, A. Mattox, R. H. Hruban, C. L. Wolfgang, M. G. Goggins, M. D. Molin, T.-L. Wang, R. Roden, A. P. Klein, J. Ptak, L. Dobbryn, J. Schaefer, N. Silliman, M. Popoli, J. T. Vogelstein, J. D. Browne, R. E. Schoen, R. E. Brand, J. Tie, P. Gibbs, H.-L. Wong, A. S. Mansfield, J. Jen, S. M. Hanash, M. Falconi, P. J. Allen, S. Zhou, C. Bettgowda, L. A. Diaz, C. Tomasetti, K. W. Kinzler, B. Vogelstein, A. M. Lennon, N. Papadopoulos, *Science* **2018**, *359*, 926.
- [31] J. Wang, S. Chang, G. Li, Y. Sun, *Front. Med.* **2017**, *11*, 522.
- [32] V. Savinov, N. I. Zheludev, *Appl. Phys. Lett.* **2017**, *111*, 091106.
- [33] J. Yang, I. Ghimire, P. C. Wu, S. Gurung, C. Arndt, D. P. Tsai, H. W. H. Lee, *Nanophotonics* **2019**, *8*, 443.
- [34] A. Xomalis, I. Demirtzioglou, E. Plum, Y. Jung, V. Nalla, C. Lacava, K. F. Macdonald, P. Petropoulos, D. J. Richardson, N. I. Zheludev, *Nat. Commun.* **2018**, *9*, 182.
- [35] H. Pahlevaninezhad, M. Khorasaninejad, Y.-W. Huang, Z. Shi, L. P. Hariri, D. C. Adams, C.-W. Qiu, F. Capasso, M. J. Suter, in *Optical Coherence Tomography and Coherence Domain Optical Methods in Biomedicine XXIII* (Eds: J. G. Fujimoto, J. A. Izatt), SPIE **2019**.
- [36] S. Larouche, D. R. Smith, *Opt. Lett.* **2012**, *37*, 2391.
- [37] M. Berry, *J. Mod. Opt.* **1987**, *34*, 1401.
- [38] A. Ricciardi, M. Consales, G. Quero, A. Crescitelli, E. Esposito, A. Cusano, *Opt. Fiber Technol.* **2013**, *19*, 772.
- [39] A. Crescitelli, A. Ricciardi, M. Consales, E. Esposito, C. Granata, V. Galdi, A. Cutolo, A. Cusano, *Adv. Funct. Mater.* **2012**, *22*, 4389.
- [40] M. Principe, M. Consales, G. Castaldi, V. Galdi, A. Cusano, *Nanomater. Nanotechnol.* **2019**, *9*, 184798041983272.
- [41] X. Wang, L. C. Kogos, R. Paiella, *OSA Continuum* **2019**, *2*, 32.
- [42] S. Zou, N. Janel, G. C. Schatz, *J. Chem. Phys.* **2004**, *120*, 10871.
- [43] L. Zhao, K. L. Kelly, G. C. Schatz, *J. Phys. Chem. B* **2003**, *107*, 7343.
- [44] H. Gao, J. M. McMahon, M. H. Lee, J. Henzie, S. K. Gray, G. C. Schatz, T. W. Odom, *Opt. Express* **2009**, *17*, 2334.
- [45] I. Puscasu, D. Spencer, G. D. Boreman, *Appl. Opt.* **2000**, *39*, 1570.
- [46] M. G. Moharam, T. K. Gaylord, E. B. Grann, D. A. Pomet, J. Opt. Soc. Am. A **1995**, *12*, 1068.
- [47] P. B. Catrysse, S. Fan, J. Nanophotonics **2008**, *2*, 021790.
- [48] Y. Yang, I. I. Kravchenko, D. P. Briggs, J. Valentine, *Nat. Commun.* **2014**, *5*, 5753.
- [49] G. Quero, S. Zuppolini, M. Consales, L. Diodato, P. Vaiano, A. Venturelli, M. Santucci, F. Spyrikis, M. Costi, M. Giordano, A. Borriello, A. Cutolo, A. Cusano, *Sens. Actuators, B* **2016**, *230*, 510.
- [50] A. Aliberti, P. Vaiano, A. Caporale, M. Consales, M. Ruvo, A. Cusano, *Sens. Actuators, B* **2017**, *247*, 727.
- [51] V. Voisin, J. Pilate, P. Damman, P. Mégret, C. Caucheteur, *Biosens. Bioelectron.* **2014**, *51*, 249.

- [52] L. Liu, L. Marques, R. Correia, S. P. Morgan, S.-W. Lee, P. Tighe, L. Fairclough, S. Korposh, *Sens. Actuators, B* **2018**, 271, 24.
- [53] M. Wan, P. Luo, J. Jin, J. Xing, Z. Wang, S. T. C. Wong, *Sensors* **2010**, 10, 6477.
- [54] D. J. J. Hu, J. L. Lim, M. Jiang, Y. Wang, F. Luan, P. P. Shum, H. Wei, W. Tong, *Opt. Lett.* **2012**, 37, 2283.
- [55] Z. Wang, J. Heflin, K. V. Cott, R. H. Stolen, S. Ramachandran, S. Ghalmi, *Sens. Actuators, B* **2009**, 139, 618.
- [56] L. V. Nguyen, S. C. Warren-Smith, K. Hill, in *6th Int. Conf. on the Development of Biomedical Engineering in Vietnam (BME6), IFMBE Proceedings 63* (Eds: T. V. Von, T. A. Nguyen Le, T. Nguyen Duc), Springer Nature Singapore Pte Ltd. **2018**, p. 481.
- [57] N. Bhalla, P. Jolly, N. Formisano, P. Estrela, *Essays Biochem.* **2016**, 60, 1.
- [58] K. L. Adams, M. Puchades, A. G. Ewing, *Annu. Rev. Anal. Chem.* **2008**, 1, 329.
- [59] G. Quero, M. Consales, R. Severino, P. Vaiano, A. Boniello, A. Sandomenico, M. Ruvo, A. Borriello, L. Diodato, S. Zuppolini, M. Gior-
dano, I. C. Nettore, C. Mazzarella, A. Colao, P. E. Macchia, F. Santorelli, A. Cutolo, A. Cusano, *Biosens. Bioelectron.* **2016**, 80, 590.
- [60] L. Alwis, T. Sun, K. T. Grattan, *Proc. Eng.* **2012**, 47, 718.
- [61] J. Cao, M. H. Tu, T. Sun, K. T. Grattan, *Sens. Actuators, B* **2013**, 181, 611.
- [62] S. Pissadakis, *Microelectron. Eng.* **2019**, 217, 111105.
- [63] S. Mowbray, A. Amiri, *Diagnostics* **2019**, 9, 23.
- [64] J. Li, H. Ebendorff-Heidepriem, B. C. Gibson, A. D. Greentree, M. R. Hutchinson, P. Jia, R. Kostecki, G. Liu, A. Orth, M. Ploschner, E. P. Schartner, S. C. Warren-Smith, K. Zhang, G. Tsiminis, E. M. Goldys, *APL Photonics* **2018**, 3, 100902.
- [65] R. Correia, S. James, S.-W. Lee, S. P. Morgan, S. Korposh, *J. Opt.* **2018**, 20, 073003.
- [66] M. A. El-Sherif, J. Yuan, A. Macdiarmid, *J. Intell. Mater. Syst. Struct.* **2000**, 11, 407.
- [67] A. K. Yetisen, H. Qu, A. Manbachi, H. Butt, M. R. Dokmeci, J. P. Hinstroza, M. Skorobogatiy, A. Khademhosseini, S. H. Yun, *ACS Nano* **2016**, 10, 3042.